Journal of Pathology
J Pathol April 2025; **265:** 518–531
Published online 20 February 2025 in Wiley Online Library
(wileyonlinelibrary.com) DOI: 10.1002/path.6405

ORIGINAL ARTICLE

Spatial profiling of *ANO7* in prostate tissue: links to AR-signalling-associated lipid metabolism and inflammation

Olli Metsälä[1,2], Gudrun Wahlström[1,2], Neha Goel[1,2], Mitro Miihkinen[3,4], Pekka Taimen[1,2,5] and Johanna Schleutker[1,2,6*]

[1] *Institute of Biomedicine, University of Turku, Turku, Finland*
[2] *FICAN West Cancer Center, University of Turku and Turku University Hospital, Turku, Finland*
[3] *Institute for Molecular Medicine Finland (FIMM), HiLIFE, University of Helsinki, Helsinki, Finland*
[4] *iCAN Digital Precision Cancer Medicine Flagship, University of Helsinki and Helsinki University Hospital, Helsinki, Finland*
[5] *Department of Pathology, Laboratory Division, Turku University Hospital, Turku, Finland*
[6] *Department of Genomics, Laboratory Division, Turku University Hospital, Turku, Finland*

**Correspondence to: J Schleutker, Institute of Biomedicine, University of Turku, Kiinamyllynkatu 10, 20520 Turku, Finland. E-mail: johanna.schleutker@utu.fi*

Abstract

Prostate cancer (PrCa) is highly prevalent in the Western world. Currently, however, there are many unmet needs in PrCa care, for example in distinguishing between clinically significant and indolent cases in early phases of the disease. *ANO7* is a prostate-specific gene associated with PrCa risk and prognosis, but its exact function in the prostate remains unclear. This study investigates the role of *ANO7* in benign prostatic epithelium using spatial transcriptomics by examining differences between *ANO7*-expressing and non-expressing epithelial regions and their corresponding stromal compartments. A total of 18,676 protein-coding genes were assessed from prostatectomy samples collected from patients with localised prostate cancer. In the collected sample cohort, ANO7 exhibited a distinct, heterogeneous, on–off epithelial expression pattern, enabling an in-depth analysis of ANO7-dependent processes. *ANO7*-positive epithelium was predominantly enriched with luminal epithelial cells and a specific NK cell subtype, CD56bright. In contrast, *ANO7*-negative regions were characterised by enrichment of club cells, inflammation, and features of proliferative inflammatory atrophy. Gene-set enrichment analysis revealed that *ANO7* expression is associated with androgen receptor (AR) signalling and lipid metabolism. A detailed analysis of differentially expressed genes identified an ANO7- signature, which consisted of genes co-expressed with *ANO7* in luminal cells, that demonstrated high consistency in bulk RNA-sequencing (RNA-seq) data. The ANO7-signature was enriched for AR-regulated genes, which highlighted lipid metabolism processes, particularly arachidonic acid metabolism, as a key metabolic feature of the *ANO7*-positive epithelium. Furthermore, the ANO7-signature demonstrated clinical significance in low-grade PrCa, correlating with a better response to therapy. In summary, these results highlight the potential role of *ANO7* in regulating lipid metabolism associated with androgen signalling in benign luminal cells and low-grade cancer, reinforcing the hypothesis that *ANO7* functions as a tumour suppressor.

Keywords: spatial transcriptomics; prostate; *ANO7*; luminal cell; AR signalling; lipid metabolism

Received 22 October 2024; Revised 18 December 2024; Accepted 15 January 2025

No conflicts of interest were declared.

Introduction

Prostate cancer (PrCa) imposes a substantial burden on healthcare systems globally. However, current treatment options for localised PrCa, such as surgery, radiation therapy, or active surveillance, do not show significant differences in cancer-specific survival rates [1]. *ANO7* (anoctamin 7), a gene highly expressed in the prostate, has emerged as a potential candidate for PrCa prognostication. ANO7 belongs to the anoctamin family of transmembrane proteins (ANO1–10), which act as Ca^{2+}-activated ion channels or lipid scramblases [2]. Notably, reduced ANO7 protein levels correlate with poor prognosis [3], and *ANO7* is included in the Decipher biomarker panel for predicting the risk of developing aggressive PrCa [4]. Certain inherited variants in *ANO7* are associated with an increased risk for PrCa [5]. We have characterised the single nucleotide polymorphism (SNP) rs77559646, which causes defective mRNA splicing and loss of protein in men homozygous for that SNP [6,7]. Recently, *ANO7* was detected as an important risk gene in men of African ancestry [8,9]. Despite its association with PrCa, the exact function of *ANO7* in the prostate remains unknown. We and

others hypothesise that *ANO7* might function as a tumour suppressor [3,6].

This study explores the role of *ANO7* in the prostate epithelium, cataloguing the processes and mechanisms in which *ANO7* is involved. Given that tissue changes during cancer progression involve reduced *ANO7* expression [10,11], we chose to investigate a benign setting to focus specifically on processes related to *ANO7* function, rather than confounding them with general tumour progression. For analysis, we employed the GeoMx Digital Spatial Profiler (DSP), chosen for its capability to allow manual selection of regions of interest (ROIs) and to retain information about the exact location of the cells within the tissue [12]. We examined the differences between *ANO7*-expressing and non-expressing benign epithelium in human prostate tissue, along with the adjacent stromal compartments. This work provides a foundation and framework for studying the mechanism of action of *ANO7* in benign prostatic cells and in PrCa.

Materials and methods

RNA fluorescence *in situ* hybridization (RNA-FISH)

The probe targeted bases 1,015–1,979 in *ANO7* NCBI NM_001001891.3 as previously described [13].

Ethical approval for human prostate tissue collection

All the patients gave written and signed informed consent according to the principles in the Declaration of Helsinki. The research was approved by the Institutional Review Board of the Turku University Hospital. Tissues were collected from radical prostatectomy specimens.

Immunostaining

Formalin-fixed, paraffin-embedded (FFPE) sections were subjected to immunohistochemical (IHC) staining for samples utilised in RNA-FISH. Fresh-frozen (FF) sections were used for GeoMx DSP (NanoString Technologies, Inc., Seattle, WA, USA) and in immunofluorescence. The staining protocols have been previously described [6,14] and are also detailed in Supplementary materials and methods.

Imaging

The RNA-FISH sections were scanned using a PANNORAMIC Midi slide scanner (3DHISTECH, Budapest, Hungary), and the haematoxylin and eosin (H&E) and IHC sections were scanned using a PANNORAMIC 1000 slide scanner (3DHISTECH). Images were captured using CaseViewer (3DHISTECH). Immunofluorescence sections were imaged using a Marianas CSU-W1 spinning disc confocal microscope (3i, Denver, CO, USA). Image montages were created with SlideBook 6 software (3i) and processed using Fiji (NIH, Bethesda, MD, USA). Further details are provided in Supplementary materials and methods.

GeoMx slide preparation and sample collection

The *in situ* detection of mRNA in tissue samples was performed using the GeoMx DSP (NanoString Technologies) utilising the Whole Transcriptome Atlas [12]. Sample preparation was carried out following the manufacturer's protocol.

The ROIs in benign epithelium were selected based on the ANO7 protein staining in adjacent sections. Epithelial ROIs were manually outlined according to the pan-cytokeratin staining, and stromal ROIs were drawn outside the corresponding epithelial regions. H&E-stained sections confirmed the benignity of the glands.

The cDNA libraries were prepared by the Single Cell Core Unit, and sequenced by the Finnish Functional Genomics Centre at Turku Bioscience, Turku, Finland, using the NovaSeq 6000 S1 v1.5 platform (Illumina, San Diego, CA, USA), following the manufacturer's protocol.

Detailed information is provided in Supplementary materials and methods.

External data

The Cancer Genome Atlas (TCGA) prostate adenocarcinoma (PRAD) RNA-seq dataset (ID: HiSeqV2) and the corresponding phenotype information, which includes clinical data about the patients, were downloaded from UCSC Xena Browser (https://tcga.xenahubs.net). Sample IDs were matched between the RNA-seq data matrix and the phenotype file, and only samples present in both datasets were included in the analysis. A total of $n = 52$ solid tissue normal samples and $n = 497$ primary tumour samples were used for analysis.

Analysis tools

Data processing was performed using the NanoString GeomxTools package in R, following the manufacturer's instructions, with the exception of normalisation, which was done using the quantile method. The following tools were employed in downstream analysis: gene set enrichment analysis (GSEA) with MSigDB v2023.2. Hs gene-sets, single-sample GSEA (ssGSEA) performed in GenePattern [15] using single-cell data cell type markers [16,17], pathway enrichment using Enrichr [18], Chipster [19] to analyse differentially expressed genes (DEGs), and ClueGO [20] for network analysis. Statistical analyses were carried out in GraphPad Prism (10.1.2; Dotmatics, Boston, MA, USA). Detailed information is provided in Supplementary materials and methods.

Results

ANO7 mRNA and protein expression exhibits an on–off expression pattern in benign epithelium

Previously, we demonstrated that *ANO7* mRNA accumulates in the nuclei of luminal epithelial cells [13]. Here, we show that in benign glands, *ANO7* mRNA and protein exhibit a non-uniform, switch-like on–off expression pattern across adjacent epithelial regions (Figure 1A–C), suggesting these areas to be differentially regulated. To further investigate this phenomenon, we used the GeoMx DSP with the Whole Transcriptome Atlas, examining 18,676 protein-coding genes.

Tissue samples were obtained from $n = 16$ PrCa patients who underwent prostatectomy. Four patients exhibiting high-contrast ANO7 protein expression patterns were selected for spatial profiling, two of whom had been treated with 5-alpha reductase inhibitors (5-ARIs), known to affect gene expression and epithelial morphology [21].

In total, 96 epithelial regions classified as positive or negative for *ANO7* were collected, along with 78 stromal regions (supplementary material, Figure S1). Following quality control and filtering, 10,606 genes in 96 epithelial samples and 6,978 genes in 65 stromal samples were analysed, including eight epithelial and six stromal replicate samples.

Epithelial *ANO7* expression defines distinct cell populations

Gene expression analysis of the epithelial samples, collected as *ANO7*-positive or *ANO7*-negative, revealed that most samples segregated into these categories. However, a portion displayed intermediate *ANO7* expression levels (supplementary material, Figure S2A). Upon re-evaluation of the ANO7 protein staining, six samples containing mixed populations of ANO7-positive and ANO7-negative cells were excluded. In patient 9, areas with strong inflammation showed low *ANO7* mRNA levels despite strong staining (supplementary material, Figure S2B,C), leading to further classification into four groups: pos-norm, neg-norm, pos-infl, and neg-infl, representing *ANO7*-positive and -negative samples in regions with low and high inflammation, respectively. *ANO7* expression was the highest in pos-norm, reduced in pos-infl, and the lowest in neg-norm and neg-infl (Figure 2A and supplementary material, Figure S2D). The stromal samples were labelled according to the adjacent epithelial sample with a prefix 's' (e.g. s-pos-norm). Stromal samples from patient 9 not located next to epithelial samples were labelled as high inflammation or low inflammation, depending on the level of immune cell abundance observed in the H&E staining.

For the epithelial samples, uniform manifold approximation and projection (UMAP) dimensionality

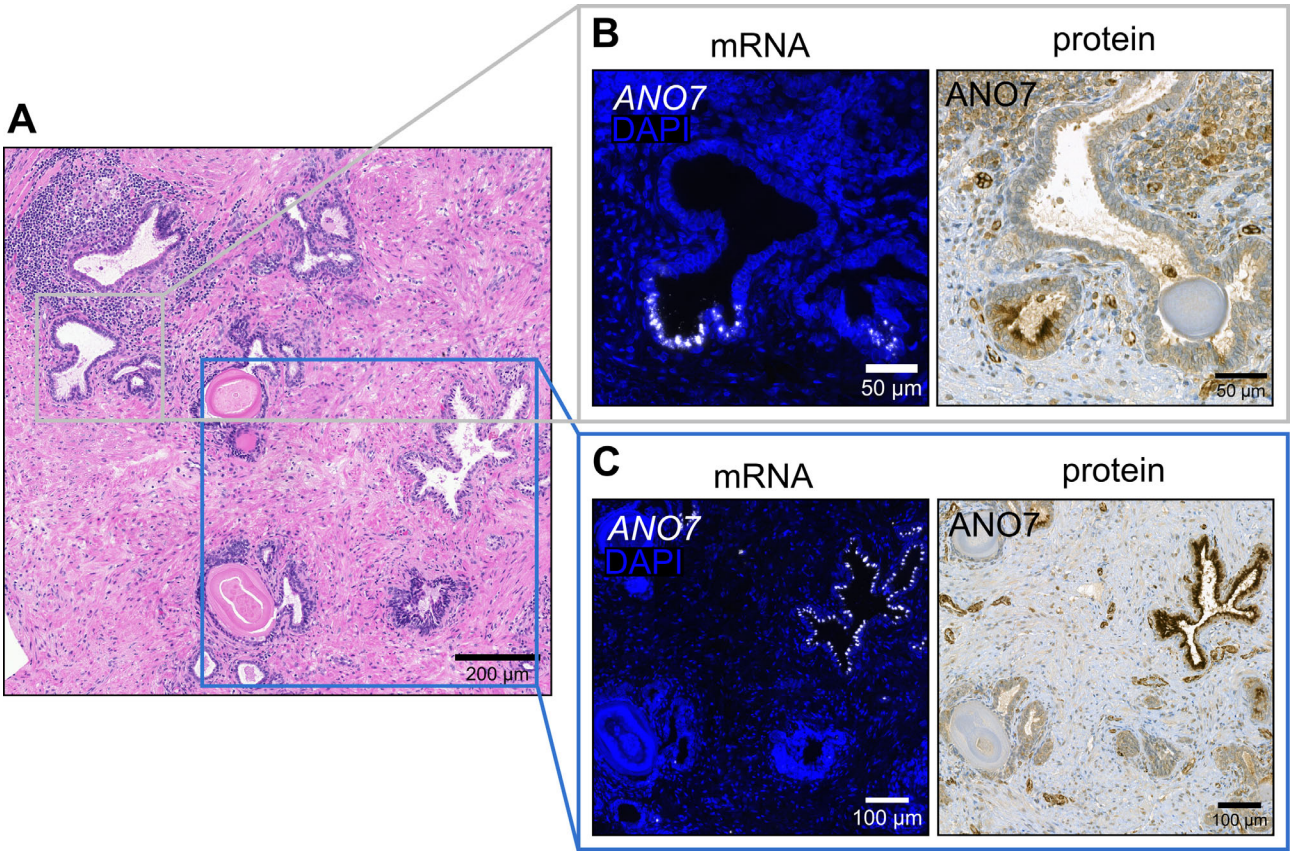

Figure 1. *ANO7* switch-like on–off expression pattern in benign prostate glands. (A) H&E staining showing the morphology of the glands. (B, C) Magnified panels showing varying expression at the mRNA and protein level within a gland (B) or between adjacent glands (C).

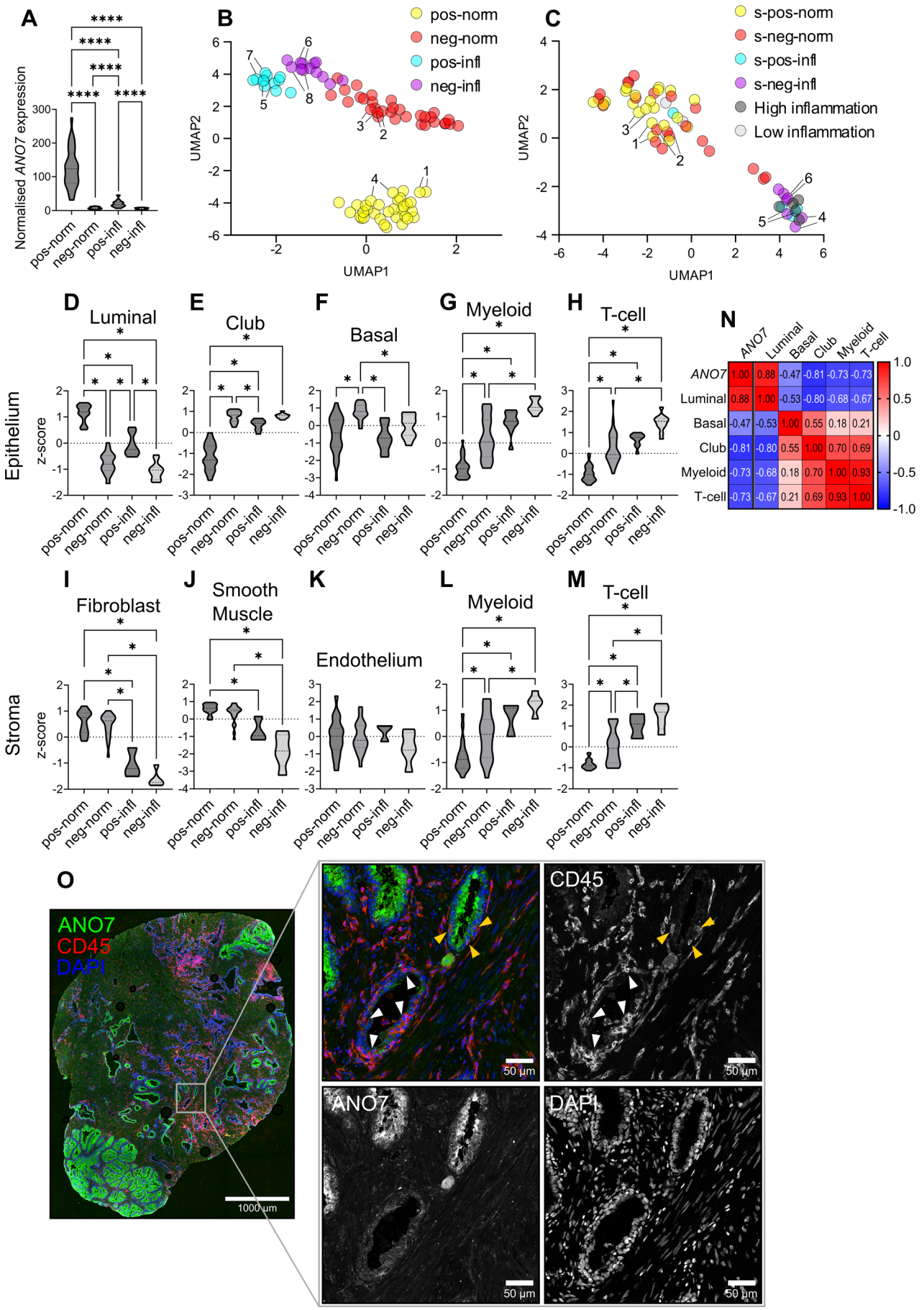

Figure 2 Legend on next page.

reduction revealed distinct clustering, with pos-norm and neg-norm samples showing clear transcriptional differences (Figure 2B). Visualisation of the clusters by patient highlighted individual variability (supplementary material, Figure S3A). The pos-infl and neg-infl samples from patient 9 clustered near the neg-norm samples, forming a continuum of *ANO7*-negative samples separated from the pos-infl cluster (Figure 2B). Thus, the samples from patient 9 formed four separate clusters, underscoring differences between regions with high and low inflammation. The two patients treated with 5-ARIs showed a slight differentiation within the pos-norm group (supplementary material, Figure S3B); however, *ANO7* expression did not significantly differ between the treated and the untreated patients (supplementary material, Figure S3C,D). Thus, 5-ARI treatment was not used as a stratifying factor in the subsequent analyses.

In the stromal dataset, the UMAP dimensionality reduction revealed two major clusters. The stromal sample groups s-pos-norm and s-neg-norm overlapped with the low inflammation samples, while s-pos-infl and s-neg-infl overlapped with the high inflammation samples (Figure 2C). These patterns suggest that immune cell abundance drives the clustering of the stromal samples. The samples from the low inflammation regions co-clustered regardless of the *ANO7* status (Figure 2C); however, the clustering was affected by variation between the individuals (supplementary material, Figure S3E). Furthermore, 5-ARI-treated and untreated samples within the low inflammation group formed distinct clusters, indicating that diminished dihydrotestosterone (DHT) levels influenced the stroma independently of the *ANO7* status in the epithelium (supplementary material, Figure S3F).

ANO7 expression is highly specific to luminal epithelial cells and shows an inverse relationship with immune cell infiltration in the epithelium

With the sample groups established, we next assessed the cell type composition of 82 epithelial and 54 stromal samples (excluding mixed and replicates) using ssGSEA. The analysis was based on cell type markers relevant to benign glands and stroma from a single-cell study on tissues containing cancer and benign glands from patients with localised PrCa [16].

The *ANO7*-positive epithelium in the low inflammation region (pos-norm) was highly enriched for luminal cells. An enrichment was not seen in pos-infl; still, both pos-norm and pos-infl showed significantly higher scores compared with neg-norm and neg-infl (Figure 2D). The *ANO7*-negative epithelium (neg-norm, neg-infl) as well as the *ANO7*-positive epithelium from high inflammation regions (pos-infl) was enriched with club cells (Figure 2E). Basal cells were more abundant in neg-norm compared with the other groups (Figure 2F). The myeloid and T-cell scores were the lowest in pos-norm, progressively higher in neg-norm and pos-infl, and reached their highest levels in neg-infl (Figure 2G,H).

In the stroma, fibroblasts and smooth muscle cells were equally abundant in s-pos-norm and s-neg-norm but reduced in s-pos-infl and s-neg-infl (Figure 2I,J). The endothelium scores were the same in all groups (Figure 2K). The myeloid and T-cell scores displayed an inverse relationship with the fibroblast and smooth muscle scores, with a pattern reflected within the epithelium (Figure 2L,M). This confirms that immune cell abundance primarily drives the clustering of the stromal samples (Figure 2C).

The luminal cell scores strongly correlated with *ANO7* expression across all epithelial samples, whereas the inverse correlation between *ANO7* expression and club cell identity mirrored the relationship between luminal and club cells (Figure 2N). The intermediate luminal and club scores of pos-infl suggest a luminal-to-club cell transition in the *ANO7*-positive epithelium in high inflammation regions. This process has previously been observed in non-cancerous prostate tissue from patients on 5-ARI medication [21]. However, in our data, the transition appears to be linked to immune cell abundance, as the high inflammation samples came from an untreated individual.

To confirm the results indicating varying quantities of immune cells within the epithelium, we performed immunofluorescence staining using antibodies against ANO7 and leukocyte common antigen CD45 for immune cell detection [22]. The result showed that regions with a high density of CD45-positive cells contained mostly ANO7-negative glandular epithelia (Figure 2O and supplementary material, Figure S4A–H). Immune cells were seen to infiltrate the epithelium in ANO7-negative glands, even reaching the lumen. In contrast, ANO7-positive glands were surrounded by immune cells, with only a few CD45-positive cells infiltrating the epithelium (Figure 2O). These findings support the immune cell detection observed in the ssGSEA cell type analysis.

Differential gene expression analysis between pos-norm and neg-norm, and between pos-infl and neg-infl,

Figure 2. Sample characterisation and cell type analysis. (A) *ANO7* expression in the sample groups (****FDR < 0.0001 in limma). (B, C) Uniform manifold approximation and projection (UMAP) plot by sample group for epithelium (B) and stroma (C). The numbers mark the replicate samples in B (1–8) and C (1–6) that co-localise in the plots, thereby demonstrating robustness of the data. (D–H) Cell composition analysis in the epithelial samples for different cell types: luminal (D), club (E), basal (F), myeloid (G), and T-cells (H). *FDR < 0.05. (I–M) Cell composition analysis in the stromal samples for different cell types: fibroblast (I), smooth muscle (J), endothelium (K), myeloid (L), and T-cells (M). *FDR < 0.05. (N) Correlation matrix of the analysed epithelial cell types, including *ANO7* expression. (O) Antibody staining for ANO7 (green) and CD45 (red). DAPI (blue) marks the nuclei. The magnified panels show adjacent ANO7-positive and ANO7-negative glands. CD45-positive cells infiltrating the epithelium are marked with yellow arrowheads in the ANO7-positive gland and white arrowheads in the ANO7-negative gland.

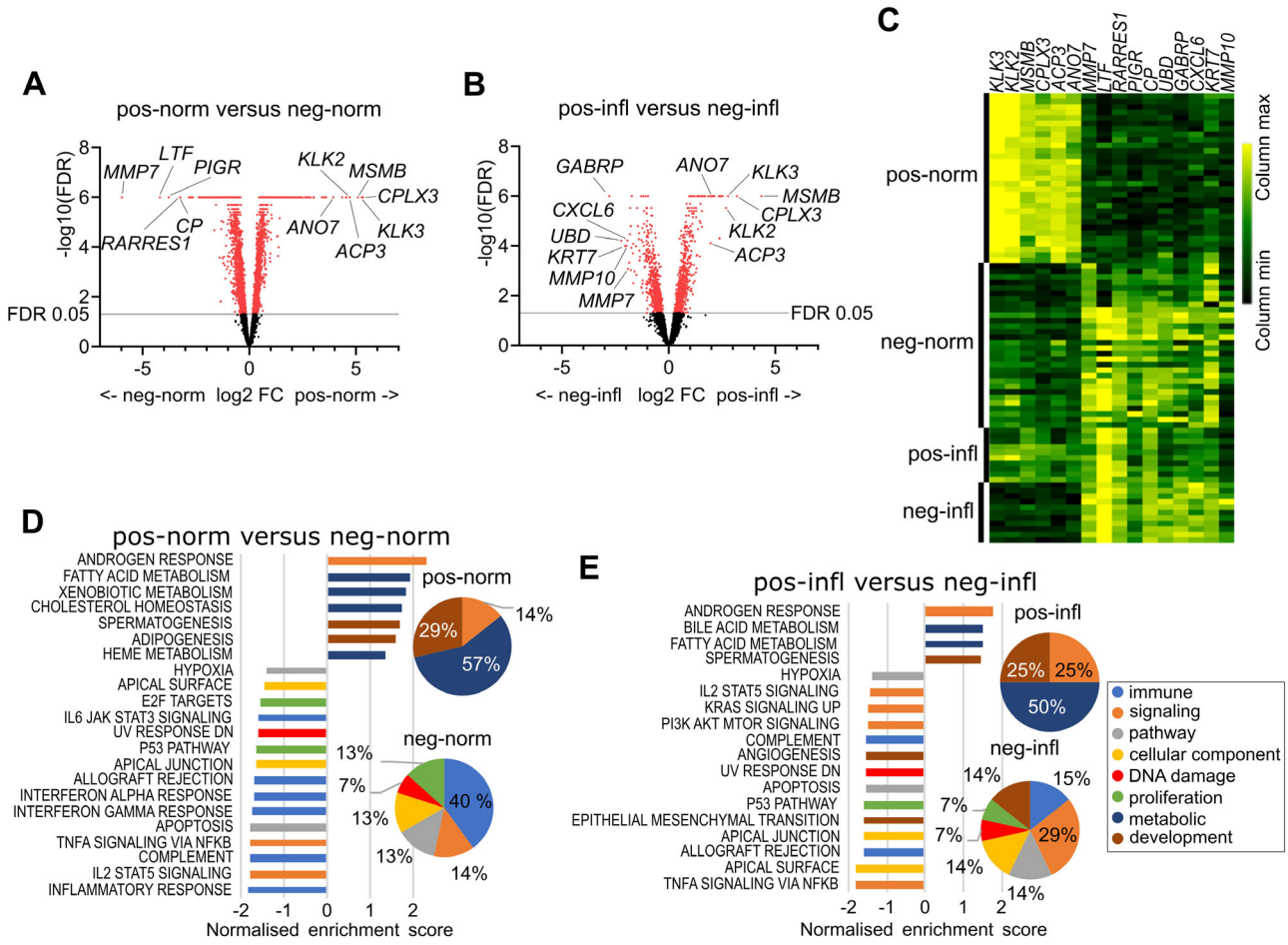

Figure 3. Differential gene expression and gene-set enrichment analysis in the epithelial samples. (A) DEGs in *ANO7*-positive (pos-norm) versus *ANO7*-negative (neg-norm) samples. (B) DEGs in *ANO7*-positive (pos-infl) versus *ANO7*-negative (neg-infl) samples in the high inflammation regions. (A, B) Selected DEGs highlight the enrichment of luminal marker genes in *ANO7*-positive samples and the variation of the top DEGs in *ANO7*-negative samples. (C) Heatmap of log_2-transformed expression values for the DEGs indicated in A and B. (D, E) GSEA showing Hallmark gene-sets enriched in pos-norm versus neg-norm samples (D) and pos-infl versus neg-infl samples (E) (nominal p value < 0.05, FDR < 0.25). Hallmark gene-sets are coloured according to the process category and the proportions of the categories are shown in D and E.

revealed 3,778 and 1,815 DEGs, respectively [false discovery rate (FDR) < 0.05] (Figure 3A,B and supplementary material, Table S2). In pos-norm, the top DEGs with the highest fold-changes were luminal cell markers such as *CPLX3*, *KLK3*, *MSMB*, *ACP3*, and *KLK2*, while in neg-norm, the club cell markers *MMP7*, *LTF*, *PIGR*, *RARRES1*, and *CP* were prominent (Figure 3A) [16,21,23]. Also, in pos-infl, the above-mentioned luminal cell markers were among the top DEGs (Figure 3B). *ANO7* was enriched with a binary logarithmic fold-change (log_2 FC) of 3.93 in pos-norm versus neg-norm but only with log_2 FC of 1.99 in pos-infl versus neg-infl (Figure 3A,B and supplementary material, Table S2). The luminal marker genes showed a similar lower level of enrichment in pos-infl compared with pos-norm, reflecting the lower luminal cell scores in pos-infl compared with pos-norm in the ssGSEA (Figure 2D). Of the top DEGs in neg-norm, only *MMP7* was differentially expressed also in neg-infl, while *LTF*, *PIGR*, *RARRES1*, and *CP* were prominently expressed in both pos-infl and neg-infl (Figure 3C). These results suggest that the pos-infl epithelia exhibit both luminal and club cell transcriptional programmes in parallel, as seen in the ssGSEA analysis.

Androgen response and metabolism-related pathways are enriched in the *ANO7*-positive epithelium

To differentiate the pathways in *ANO7*-positive and *ANO7*-negative epithelium, GSEA was conducted using the Hallmark gene-sets [24]. Comparisons between pos-norm and neg-norm and pos-infl and neg-infl (Figure 3D,E and supplementary material, Table S3) showed that androgen response was the most enriched gene-set in both *ANO7*-positive groups, accompanied by fatty acid metabolism and spermatogenesis. In contrast, inflammatory response was most enriched in neg-norm, whereas neg-infl was most enriched for TNF-α signalling via NF-κB. The lack of enriched inflammation-related gene-sets in neg-infl is likely explained by similar strong inflammatory responses in both pos-infl and neg-infl. However, enrichment of complement and allograft rejection in neg-infl indicates some immune response variation

even in high inflammation regions. In summary, androgen signalling and metabolic pathways in *ANO7*-positive epithelium versus TNF-α signalling in *ANO7*-negative epithelium constitutes the key difference between *ANO7*-positive and -negative epithelia across inflammation levels. These findings highlight the link between *ANO7* expression, androgen signalling, and metabolism in the prostate epithelium.

ANO7-signature genes function in monoamine transport, prostate glandular epithelium development, AR-regulated gene expression, and arachidonic acid metabolism

To better understand the processes involving *ANO7*, we conducted an in-depth analysis of *ANO7*-associated genes using a gene-set network approach. We focused on genes upregulated in *ANO7*-positive samples from the low inflammation regions. To account for patient-specific variation, we performed patient-wise differential gene expression analyses (pos-norm versus neg-norm), compiling 277 upregulated and 183 downregulated genes (FDR < 0.05 in all analyses) (supplementary material, Table S4). Correlation analysis between *ANO7* and the upregulated genes in the pos-norm samples identified 99 genes being co-expressed with *ANO7* ($r > 0.4$, $p < 0.05$), forming the ANO7-signature (Figure 4A and supplementary material, Table S5). The ANO7-signature includes genes associated with androgen signalling and lipid metabolism that are linked to prostate cancer, such as *AR*, *KLK3*, *SPDEF*, *FASN*, *FAAH*, *EPHX2*, *ALOX15B*, and *PLA2G4F* [25–30].

To validate the ANO7-signature, we assessed the correlation between *ANO7* expression and the signature in solid tissue normal (STN) samples from the TCGA PRAD data. The correlation was strong ($r = 0.90$), closely aligning with that in the GeoMx DSP epithelial samples ($r = 0.93$) (Table 1), indicating that ANO7-signature genes are strongly co-expressed with *ANO7* in benign epithelium.

Next, we performed an enrichment analysis using Gene Ontologies, KEGG, and Reactome with the 277 genes upregulated in the pos-norm samples. These genes were assigned into two groups: ANO7-signature genes and the remaining upregulated genes that did not correlate with *ANO7*. Enriched terms were visualised as a functionally organised network (supplementary material, Figure S5 and Table S6). The terms including ANO7-signature genes, partitioned into functional groups, are highlighted in Figure 4B.

The enriched processes in which the ANO7-signature genes constituted a major fraction were monoamine transport, arachidonic acid (AA) metabolism, prostate gland development, and glandular epithelial cell development, as well as two terms linked to PKN1 and AR regulation of KLK2 and KLK3 (Figure 4B). *FASN* and *SREBF1* were the central links between the development (prostate gland, glandular epithelial cell) and metabolic processes (supplementary material, Figure S5). Notably, the lipid-related clusters SREBP (sterol regulatory element-binding protein)-regulated metabolism, lipid and amino acid metabolism, and AA metabolism formed a larger entity (Figure 4B). This further illustrates the involvement of *ANO7* in androgen response pathways, SREBP-regulated fatty acid metabolism, and fatty acid derivative processing such as AA metabolism.

The link between *ANO7*, androgen signalling, and metabolism diminishes during cancer progression

We further investigated the correlation between *ANO7* expression and the ANO7-signature in TCGA PRAD samples across Gleason scores. The correlation decreased with advancing tumour grade (Table 1), suggesting that the relevance of the ANO7-signature diminishes as cancer progresses.

To identify pathways associated with *ANO7* in cancer, we generated correlation signatures for *ANO7* in the STN and each Gleason score group (supplementary material, Table S7). This involved identifying DEGs that were upregulated in the top quartile versus bottom quartile by *ANO7* expression and positively correlated ($r > 0.4$) with *ANO7* within the group (supplementary material, Figure S6). These correlation signatures were then subjected to pathway enrichment analysis using Enrichr with HALLMARK, KEGG, and Reactome libraries. The results demonstrated concordance between the GeoMx DSP network analysis and the pathways enriched in STN, with several pathways related to metabolism and androgen response. In Gleason score 6, only androgen response was enriched, whereas in Gleason score 7, no pathways were enriched. Gleason scores 8 and 9–10 showed enrichment for processes related to metallothioneins in addition to some metabolic pathways (Table 2 and supplementary material, Table S8).

Given that low *ANO7* expression in PrCa is linked to poor prognosis, we explored whether the ANO7-signature correlates with clinical parameters in PrCa using primary tumour samples from the TCGA dataset. The ANO7-signature score was calculated for each patient in the TCGA PRAD RNA-seq data, and the patients were divided into high and low ANO7-signature groups based on the zero-crossing of the signature *z*-score. Clinical comparisons showed that patients in the high ANO7-signature group were younger at diagnosis (median 1-year difference), and had lower Gleason scores and T- and N-stages. Additionally, the high ANO7-signature group had a more favourable response to primary therapy (Table 3).

CD56bright NK cells are enriched in *ANO7*-positive epithelium

For a comprehensive characterisation of immune cell composition, ssGSEA was performed using 28 pan-

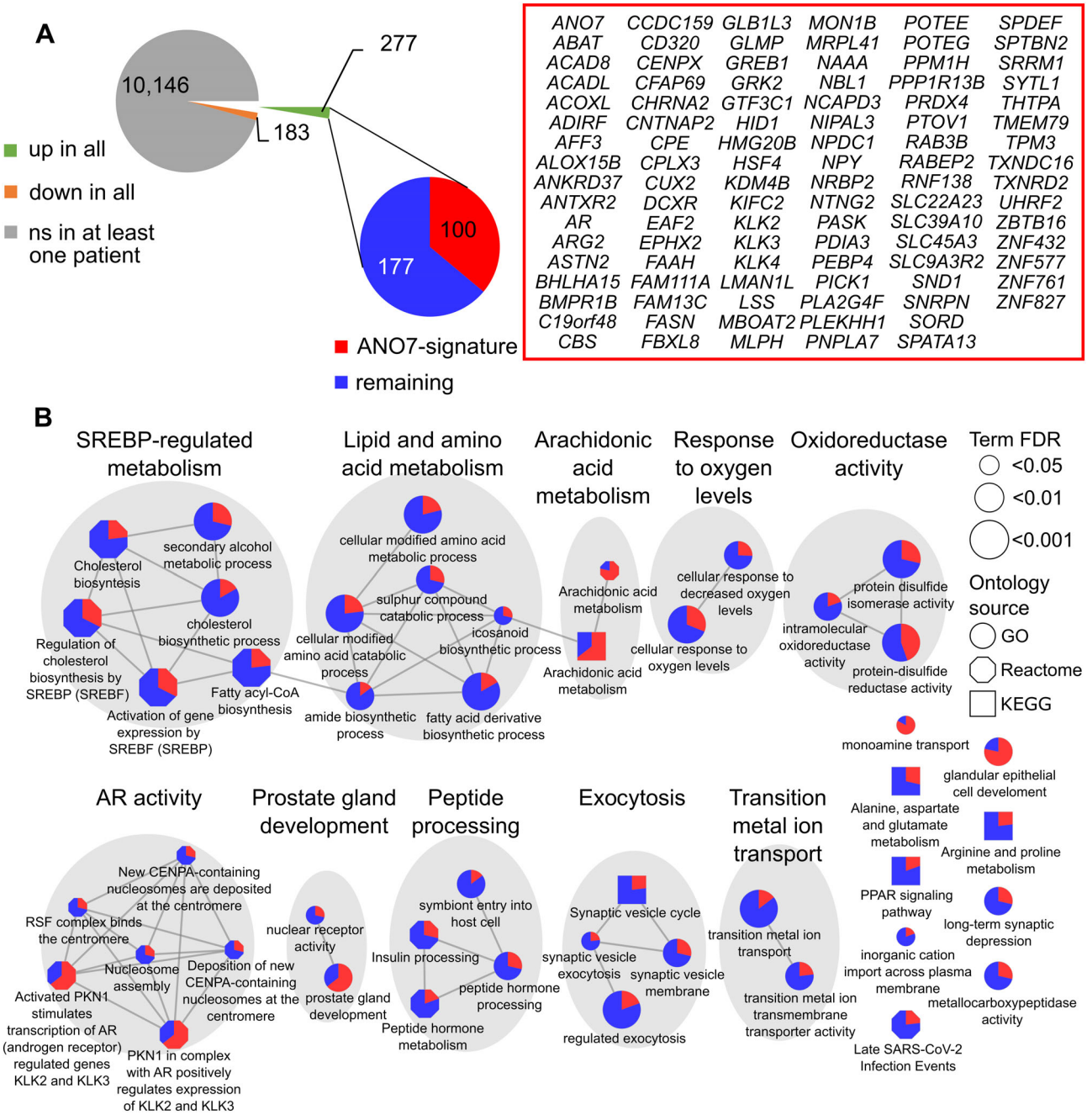

Figure 4. ANO7-signature and network analysis. (A) Differential gene expression analysis performed on pos-norm versus neg-norm in all four patients separately identified a common set of 277 upregulated and 183 downregulated genes (FDR < 0.05 in all patients). Of the upregulated genes, 99 were co-expressed with *ANO7* in the *ANO7*-positive (pos-norm) samples, constituting the ANO7-signature. (B) Network analysis terms containing ANO7-signature genes. The full network based on all 277 genes is presented in supplementary material, Figure S5 and Table S7; here, only terms containing ANO7-signature genes are shown. The colours indicate the proportion of enrichment-contributing genes in each term, with ANO7-signature genes shown in red and the remainder of the upregulated genes in blue. Edges between nodes represent connectivity based on shared genes (Cohen's kappa score ≥ 0.4). The terms are clustered using the Markov clustering algorithm. The clusters are displayed in grey and named to summarise the included terms with an emphasis on significance. Node size indicates significance, and shape denotes the ontology source.

cancer immune cell types [17]. Most cell types followed a pattern similar to that of myeloid cells and T-cells (Figure 2G,H and supplementary material, Figure S7). However, three cell types were specifically associated with *ANO7* expression: CD56bright NK cells had significantly higher scores in *ANO7*-positive epithelial samples (Figure 5A), while Th2 (type 2 T helper cells) and central memory CD8 T-cells showed higher scores in *ANO7*-negative epithelial samples (Figure 5B,C). Similar associations were not observed in the stroma (Figure 5A–C), suggesting that these immune cells selectively infiltrate the epithelium.

A similarity matrix with hierarchical clustering of immune cell ssGSEA scores of all GeoMx DSP epithelial samples, along with the ANO7-signature, showed that CD56bright NK cells and monocytes clustered with

Table 1. Correlation between *ANO7* expression and the ANO7-signature.

	r	*p* value
DSP epithelium ($n = 82$)	0.93	2.83E-35
TCGA PRAD		
STN ($n = 52$)	0.90	7.47E-20
Gleason 6 ($n = 45$)	0.74	7.16E-09
Gleason 7 ($n = 247$)	0.58	9.10E-24
Gleason 8 ($n = 64$)	0.65	4.62E-09
Gleason 9–10 ($n = 141$)	0.47	4.62E-09

Abbreviations: DSP, GeoMx Digital Spatial Profiler; STN, solid tissue normal; TCGA PRAD, The Cancer Genome Atlas prostate adenocarcinoma.

Table 2. Top pathways enriched with genes correlating with *ANO7* in the TCGA PRAD data.

Term	Combined score
Solid tissue normal (STN)	
Metallothioneins binding metals	539
Cholesterol biosynthesis	324
Androgen response	278
Response to metal ions	264
Steroid biosynthesis	172
Gleason 6	
Androgen response	48
Gleason 7	
–	
Gleason 8	
Metallothioneins binding metals	2,178
Response to metal ions	1,339
Mineral absorption	121
Bile acid metabolism	43
Gleason 9–10	
Metallothioneins binding metals	1,725
Response to metal ions	1,224
Keratan sulphate degradation	1,111
Induction of cell–cell fusion	748
Butanoate metabolism	474

Abbreviation: TCGA PRAD, The Cancer Genome Atlas prostate adenocarcinoma.

the ANO7-signature, separated from the other immune cells (Figure 5D). Monocytes, however, were not differentially distributed between the groups (supplementary material, Figure S7), making CD56bright NK cells the primary immune cell type associated with *ANO7* in luminal-type epithelium in the GeoMx DSP data.

To validate this finding, we repeated the analysis using the TCGA PRAD STN dataset. Hierarchical clustering showed that the ANO7-signature clustered with CD56bright NK cells, monocytes, activated CD8 T-cells, and CD56dim NK cells (Figure 5E). A positive correlation between the ANO7-signature and CD56bright NK cells was confirmed in both the GeoMx DSP epithelial and TCGA PRAD STN datasets ($p < 0.05$). No other cell type showed a significant correlation in both datasets (Table 4). This suggests that *ANO7*-positive epithelia are associated with changes in the tissue immune landscape via increased infiltration of specifically CD56bright NK cells.

Discussion

This study, using spatial transcriptomics, demonstrates that *ANO7* defines distinct cell populations, differentiating between luminal and club cells in benign prostatic epithelium. The *ANO7* gene expression signature is linked to AR signalling and lipid metabolism in luminal cells, enriched in low-grade cancer, and associated with a better treatment response. We also observed a positive correlation between *ANO7*-negative club cells in the epithelium and immune cell abundance in both epithelium and stroma. In contrast, CD56bright NK cells were specifically associated with the *ANO7*-positive luminal cells and the ANO7-signature.

Table 3. ANO7-signature clinical significance.

Parameter	No. of patients per ANO7-signature group						Test	*p* value
Age at initial pathologic diagnosis			Min	Max	Median		Mann–Whitney *U*	0.02
	High ($n = 273$)		41	77	61			
	Low ($n = 224$)		44	78	62			
Gleason score		Gleason 6	Gleason 7	Gleason 8	Gleason 9	Gleason 10	Fisher's exact	>0.0001
	High ($n = 273$)	33	164	31	45	0		
	Low ($n = 224$)	12	83	33	92	4		
Pathologic T*			pT2	pT3	pT4		Fisher's exact	>0.0001
	High ($n = 270$)		138	129	3			
	Low ($n = 220$)		49	164	7			
Pathologic N†			pN0	pN1			Fisher's exact	0.0017
	High ($n = 225$)		196	29				
	Low ($n = 199$)		149	50				
Primary therapy outcome success		Complete remission/ response	Partial remission/ response	Stable disease	Progressive disease		Fisher's exact	0.005
	High ($n = 210$)	178	9	14	9			
	Low ($n = 167$)	118	8	27	14			

*Pathologic *T* value, simplified to pT2–4, indicates the extent of the tumour (pT2: organ confined; pT3–4: growth beyond the prostate).
†Pathologic *N* value indicates the presence (pN1) or absence (pN0) of cancer cells in nearby lymph nodes.

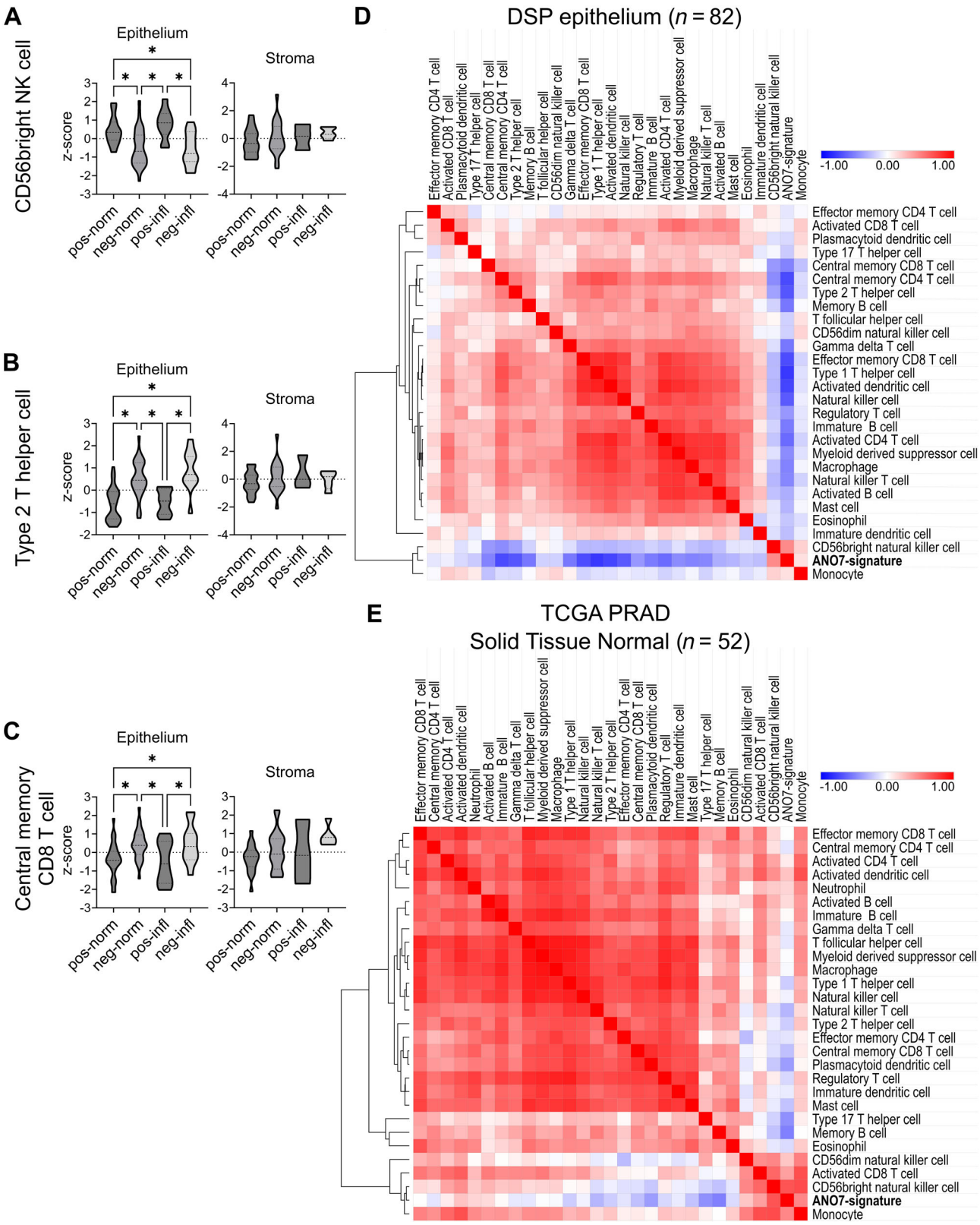

Figure 5. Immune cell analysis using the GeoMx DSP and TCGA PRAD data. (A–C) Composition of the following immune cell types per group in the epithelium and stroma: CD56bright NK cells (A), Th2 (B), and central memory CD8 T-cells (C). The CD56bright NK cells are enriched in both *ANO7*-positive groups, while Th2 and central memory CD8 T-cells are enriched in both *ANO7*-negative groups (*FDR < 0.05). The correlation is seen only in the epithelial samples. (D, E) Hierarchically clustered correlation matrix of the ssGSEA scores for the ANO7-signature and (D) $n = 27$ immune cell types in the GeoMx Digital Spatial Profiler (DSP) epithelial data and (E) $n = 28$ immune cell types in The Cancer Genome Atlas (TCGA) prostate adenocarcinoma (PRAD) solid tissue normal (STN) data. The ANO7-signature clustered closest to CD56bright NK cell in both datasets, separately from the majority of the other immune cell types.

Table 4. Correlation between the ANO7-signature and immune cell types.

	DSP epithelium ($n = 82$)		TCGA PRAD STN ($n = 52$)	
	r	*p* value	*r*	*p* value
CD56bright NK cell	0.46	1.41E-5	0.67	5.27E-8
Monocyte	0.121	0.281	0.47	4.30E-4
Activated CD8 T-cell	−0.07	0.561	0.37	0.007
CD56dim NK cell	−0.18	0.102	0.22	0.111
Th2	−0.66	1.20E-11	−0.20	0.162
Central memory CD8 T-cell	−0.49	3.96E-6	−0.25	0.076

Abbreviations: DSP, GeoMx Digital Spatial Profiler; TCGA PRAD STN, The Cancer Genome Atlas prostate adenocarcinoma solid tissue normal.

Healthy prostate epithelium consists primarily of luminal and basal cells, with club and hillock cells more prevalent in the transition and central zones [31]. Luminal cells, which express high levels of AR-regulated proteins such as KLK2 and KLK3, are secretory cells adapted for citrate production [32]. Club cells, originally identified in the lungs, play a role in host defence and are linked to proliferative inflammatory atrophy in response to injury [23,31,33]. They are characterised by the expression of *PIGR*, *CP*, *LTF*, and *MMP7*, and by the enrichment of NF-κB pathway genes [21,23].

Our findings are consistent with these characteristics, with *ANO7*-negative epithelia being marked by club cell marker genes and NF-κB signalling, while *ANO7*-positive epithelia express luminal markers and exhibit androgen response. Although a previous spatial sequencing study suggested that club cells emerge due to DHT deprivation resulting from 5-ARI treatment [21], our data indicate the presence of club cells in both 5-ARI-treated and untreated patients. This finding, together with the strong association between club cells and immune cells, implies that the emergence of club cells may be driven also by inflammation [34]. Additionally, AR and NF-κB signalling are not mutually exclusive; the pathways rather interact indirectly via shared transcription factors, thereby activating a transcriptome distinct from that induced by either pathway alone [35]. Thus, reduced AR activity followed by DHT deprivation likely renders the epithelium more susceptible to club cell adaptation in response to milder external cues inducing inflammation.

In this study, *ANO7* is strongly associated with luminal cell identity, which is linked to fatty acid and amino acid metabolism as well as oxidative phosphorylation. Interference with mitochondrial function resulting in accumulation of lactate is shown to antagonise luminal cell identity [36]. The network analysis provides a detailed representation of the cellular processes linked to *ANO7* expression. Enriched terms in the ANO7-signature are associated with AR signalling, particularly within the functional groups AR activity and prostate gland development, which suggests a link between *ANO7* expression and AR signalling in luminal cells. Notably, *ANO7* expression was shown to increase following androgen treatment in androgen-sensitive LNCaP cells [37]. In the network, the development-related processes, SREBP-regulated lipid metabolism, and *FASN* form an intriguing axis. *SREBF1* regulates fatty acid synthesis in normal tissue, whereas in cancer, *SREBF1* and androgens create a positive feedback loop that enhances fatty acid synthesis, in which *FASN* is essential [26,38]. ANO7-signature genes were also enriched in AA metabolism, which plays a significant role in the development and progression of PrCa [39–41]. Beyond cancer, AA metabolites are also essential in immune responses, affecting inflammation, immune cell function, and disease progression in various tissues [42]. Thus, lipid metabolism appears central to the role of *ANO7* in benign tissue, a conclusion also supported by the TCGA PRAD STN data.

The ANO7-signature is linked to CD56bright NK cells, a highly cytokine-secreting but less cytotoxic NK cell type compared with CD56dim NK cells. INF-γ released by CD56bright NK cells promotes immunosuppression in the tumour microenvironment [43]. In contrast, an enrichment of more cytotoxic CD56dim NK cells is associated with a better survival in osteosarcoma and melanoma [43]. Furthermore, increased lipid metabolism is shown to reduce NK cell INF-γ production in lymphoma [44]. Further research is needed to explore a possible connection between *ANO7*-related processes and NK cell function in the tissue.

In TCGA PRAD of all Gleason grades, a strong enrichment of lipid-related pathways was less evident, and androgen response was enriched only in Gleason grade 6 cancer. The lack of enriched pathways in Gleason grade 7 cancer is likely due to heterogeneity among the samples in the TCGA PRAD dataset. Interestingly, in both STN and high-grade cancer, metallothionein-related pathways, driven mainly by *MT1* subisoforms, correlated with *ANO7*. Decreased expression resulting from hypermethylation of several *MT1* subisoforms has been shown to be associated with PrCa progression [45–47]. Similarly, methylation of *ANO7* could offer an explanation for its downregulation during cancer progression.

Lastly, the ANO7-signature also demonstrates clinical relevance. Patients with high ANO7 -signature scores had a slightly lower age at diagnosis, suggesting that *ANO7*-related processes may contribute to faster progression at early-stage PrCa. Gleason score and tumour T- and N-stage were significantly lower in the high ANO7-signature group, which also showed a better response to primary therapy. This suggests that *ANO7*-related processes are more relevant in low-grade cancers, the metabolism of which resembles that

of benign luminal cells. In contrast, advanced cancer cells show greater metabolic plasticity [36,48,49] and no longer depend on *ANO7* function. The poor prognostic effect of reduced ANO7 protein in cancer [3] suggests that *ANO7* antagonises oncogenic lipid metabolism [26], therefore acting as a tumour suppressor.

A limitation of this study is the lack of a causal relationship between *ANO7* and the correlating genes, necessitating future biochemical analyses. Future studies should focus on modelling *ANO7* function in benign luminal or low-grade cancer cells to enable a more impactful functional analysis of *ANO7*'s role.

Acknowledgements

We are grateful to the patients at Turku University Hospital, Turku, Finland for consenting to participate in the Turku Prostate Cancer Consortium sample collection and committing to basic research. We thank the other members of the JS lab for scientific feedback and support, as well as Dr Emilia Peuhu and her lab for providing reagents and assistance with the experiments. This study was supported by the Sigrid Juselius Foundation, the Jane and Aatos Erkko Foundation (grant No. 170069), the Cancer Foundation Finland sr, and State Research Funding of Turku University Hospital. OM was supported by the Turku Doctoral Programme of Molecular Medicine, the Cancer Foundation Finland sr, and the Turku University Foundation (081755).

Author contributions statement

The study was designed by OM, GW and JS. Experiments were designed by OM, GW and JS and carried out by OM. Data processing was performed by NG. Investigation was carried out by OM, GW and MM. PT conducted pathological evaluation of the samples. OM and GW drafted the manuscript, and OM generated figures. All authors contributed to editing and approved the final manuscript. The project was supervised and funding was acquired by JS.

Data availability statement

According to the Finnish biobank practices, access to the data can be requested via Auria Biobank (https://www.auria.fi/biobank).

References

1. Hamdy FC, Donovan JL, Lane JA, *et al*. Fifteen-year outcomes after monitoring, surgery, or radiotherapy for prostate cancer. *N Engl J Med* 2023; **388:** 1547–1558.
2. Kalienkova V, Clerico Mosina V, Paulino C. The groovy TMEM16 family: molecular mechanisms of lipid scrambling and ion conduction. *J Mol Biol* 2021; **433:** 166941.
3. Marx A, Koopmann L, Höflmayer D, *et al*. Reduced anoctamin 7 (ANO7) expression is a strong and independent predictor of poor prognosis in prostate cancer. *Cancer Biol Med* 2021; **18:** 245–255.
4. Erho N, Crisan A, Vergara IA, *et al*. Discovery and validation of a prostate cancer genomic classifier that predicts early metastasis following radical prostatectomy. *PLoS One* 2013; **8:** e66855.
5. Wang A, Shen J, Rodriguez AA, *et al*. Characterizing prostate cancer risk through multi-ancestry genome-wide discovery of 187 novel risk variants. *Nat Genet* 2023; **55:** 2065–2074.
6. Wahlström G, Heron S, Knuuttila M, *et al*. The variant rs77559646 associated with aggressive prostate cancer disrupts *ANO7* mRNA splicing and protein expression. *Hum Mol Genet* 2022; **31:** 2063–2077.
7. Kaikkonen E, Rantapero T, Zhang Q, *et al*. ANO7 is associated with aggressive prostate cancer. *Int J Cancer* 2018; **143:** 2479–2487.
8. Chen F, Madduri RK, Rodriguez AA, *et al*. Evidence of novel susceptibility variants for prostate cancer and a multiancestry polygenic risk score associated with aggressive disease in men of African ancestry. *Eur Urol* 2023; **84:** 13–21.
9. Jiang J, Soh PXY, Mutambirwa SBA, *et al*. *ANO7* African-ancestral genomic diversity and advanced prostate cancer. *Prostate Cancer Prostatic Dis* 2024; **27:** 558–565.
10. Sinnott JA, Peisch SF, Tyekucheva S, *et al*. Prognostic utility of a new mRNA expression signature of Gleason score. *Clin Cancer Res* 2017; **23:** 81–87.
11. Figiel S, Yin W, Doultsinos D, *et al*. Spatial transcriptomic analysis of virtual prostate biopsy reveals confounding effect of tissue heterogeneity on genomic signatures. *Mol Cancer* 2023; **22:** 162.
12. Merritt CR, Ong GT, Church SE, *et al*. Multiplex digital spatial profiling of proteins and RNA in fixed tissue. *Nat Biotechnol* 2020; **38:** 586–599.
13. Metsälä O, Wahlström G, Taimen P, *et al*. Transcripts of the prostate cancer-associated gene *ANO7* are retained in the nuclei of prostatic epithelial cells. *Int J Mol Sci* 2023; **24:** 1052.
14. Conway JRW, Dinç DD, Follain G, *et al*. IGFBP2 secretion by mammary adipocytes limits breast cancer invasion. *Sci Adv* 2023; **9:** eadg1840.
15. Reich M, Liefeld T, Gould J, *et al*. GenePattern 2.0. *Nat Genet* 2006; **38:** 500–501.
16. Song H, Weinstein HNW, Allegakoen P, *et al*. Single-cell analysis of human primary prostate cancer reveals the heterogeneity of tumor-associated epithelial cell states. *Nat Commun* 2022; **13:** 141.
17. Charoentong P, Finotello F, Angelova M, *et al*. Pan-cancer immunogenomic analyses reveal genotype–immunophenotype relationships and predictors of response to checkpoint blockade. *Cell Rep* 2017; **18:** 248–262.
18. Kuleshov MV, Jones MR, Rouillard AD, *et al*. Enrichr: a comprehensive gene set enrichment analysis web server 2016 update. *Nucleic Acids Res* 2016; **44:** W90–W97.
19. Kallio MA, Tuimala JT, Hupponen T, *et al*. Chipster: user-friendly analysis software for microarray and other high-throughput data. *BMC Genomics* 2011; **12:** 507.
20. Bindea G, Mlecnik B, Hackl H, *et al*. ClueGO: a Cytoscape plug-in to decipher functionally grouped gene ontology and pathway annotation networks. *Bioinformatics* 2009; **25:** 1091–1093.
21. Joseph DB, Henry GH, Malewska A, *et al*. 5-Alpha reductase inhibitors induce a prostate luminal to club cell transition in human benign prostatic hyperplasia. *J Pathol* 2022; **256:** 427–441.
22. Rheinländer A, Schraven B, Bommhardt U. CD45 in human physiology and clinical medicine. *Immunol Lett* 2018; **196:** 22–32.
23. Huang FW, Song H, Weinstein HN, *et al*. Club-like cells in proliferative inflammatory atrophy of the prostate. *J Pathol* 2023; **261:** 85–95.

24. Liberzon A, Birger C, Thorvaldsdóttir H, *et al*. The Molecular Signatures Database (MSigDB) hallmark gene set collection. *Cell Syst* 2015; **1:** 417–425.
25. Vainio P, Gupta S, Ketola K, *et al*. Arachidonic acid pathway members *PLA2G7*, *HPGD*, *EPHX2*, and *CYP4F8* identified as putative novel therapeutic targets in prostate cancer. *Am J Pathol* 2011; **178:** 525–536.
26. Zadra G, Photopoulos C, Loda M. The fat side of prostate cancer. *Biochim Biophys Acta* 2013; **1831:** 1518.
27. Thors L, Bergh A, Persson E, *et al*. Fatty acid amide hydrolase in prostate cancer: association with disease severity and outcome, CB1 receptor expression and regulation by IL-4. *PLoS One* 2010; **5:** e12275.
28. Benatzy Y, Palmer MA, Brüne B. Arachidonate 15-lipoxygenase type B: regulation, function, and its role in pathophysiology. *Front Pharmacol* 2022; **13:** 1042420.
29. Whitlock NC, White ME, Capaldo BJ, *et al*. Progression of prostate cancer reprograms MYC-mediated lipid metabolism via lysine methyltransferase 2A. *Discov Oncol* 2022; **13:** 97.
30. Tsai Y-C, Chen W-Y, Abou-Kheir W, *et al*. Androgen deprivation therapy-induced epithelial–mesenchymal transition of prostate cancer through downregulating SPDEF and activating CCL2. *Biochim Biophys Acta Mol Basis Dis* 2018; **1864:** 1717–1727.
31. Henry GH, Malewska A, Joseph DB, *et al*. A cellular anatomy of the normal adult human prostate and prostatic urethra. *Cell Rep* 2018; **25:** 3530–3542.e5.
32. Ahmad F, Cherukuri MK, Choyke PL. Metabolic reprogramming in prostate cancer. *Br J Cancer* 2021; **125:** 1185–1196.
33. Zuo W-L, Shenoy SA, Li S, *et al*. Ontogeny and biology of human small airway epithelial club cells. *Am J Respir Crit Care Med* 2018; **198:** 1375–1388.
34. de Bono JS, Guo C, Gurel B, *et al*. Prostate carcinogenesis: inflammatory storms. *Nat Rev Cancer* 2020; **20:** 455–469.
35. Malinen M, Niskanen EA, Kaikkonen MU, *et al*. Crosstalk between androgen and pro-inflammatory signalling remodels androgen receptor and NF-κB cistrome to reprogram the prostate cancer cell transcriptome. *Nucleic Acids Res* 2017; **45:** 619–630.
36. Giafaglione JM, Crowell PD, Delcourt AML, *et al*. Prostate lineage-specific metabolism governs luminal differentiation and response to antiandrogen treatment. *Nat Cell Biol* 2023; **25:** 1821–1832.
37. Kiessling A, Weigle B, Fuessel S, *et al*. *D-TMPP*: a novel androgen-regulated gene preferentially expressed in prostate and prostate cancer that is the first characterized member of an eukaryotic gene family. *Prostate* 2005; **64:** 387–400.
38. Shimano H. Sterol regulatory element-binding proteins (SREBPs): transcriptional regulators of lipid synthetic genes. *Prog Lipid Res* 2001; **40:** 439–452.
39. Patel MI, Kurek C, Dong Q. The arachidonic acid pathway and its role in prostate cancer development and progression. *J Urol* 2008; **179:** 1668–1675.
40. Ghosh J, Myers CE. Inhibition of arachidonate 5-lipoxygenase triggers massive apoptosis in human prostate cancer cells. *Proc Natl Acad Sci U S A* 1998; **95:** 13182–13187.
41. Yang P, Cartwright CA, Li J, *et al*. Arachidonic acid metabolism in human prostate cancer. *Int J Oncol* 2012; **41:** 1495–1503.
42. Wang B, Wu L, Chen J, *et al*. Metabolism pathways of arachidonic acids: mechanisms and potential therapeutic targets. *Signal Transduct Target Ther* 2021; **6:** 1–30.
43. Netskar H, Pfefferle A, Goodridge JP, *et al*. Pan-cancer profiling of tumor-infiltrating natural killer cells through transcriptional reference mapping. *Nat Immunol* 2024; **25:** 1445–1459.
44. Kobayashi T, Lam PY, Jiang H, *et al*. Increased lipid metabolism impairs NK cell function and mediates adaptation to the lymphoma environment. *Blood* 2020; **136:** 3004–3017.
45. Demidenko R, Daniunaite K, Bakavicius A, *et al*. Decreased expression of *MT1E* is a potential biomarker of prostate cancer progression. *Oncotarget* 2017; **8:** 61709–61718.
46. Han Y-C, Zheng Z-L, Zuo Z-H, *et al*. Metallothionein 1 h tumour suppressor activity in prostate cancer is mediated by euchromatin methyltransferase 1. *J Pathol* 2013; **230:** 184–193.
47. Henrique R, Jerónimo C, Hoque MO, *et al*. *MT1G* hypermethylation is associated with higher tumor stage in prostate cancer. *Cancer Epidemiol Biomarkers Prev* 2005; **14:** 1274–1278.
48. Wei G, Zhu H, Zhou Y, *et al*. Single-cell sequencing revealed metabolic reprogramming and its transcription factor regulatory network in prostate cancer. *Transl Oncol* 2024; **44:** 101925.
49. Beltran H, Hruszkewycz A, Scher HI, *et al*. The role of lineage plasticity in prostate cancer therapy resistance. *Clin Cancer Res* 2019; **25:** 6916–6924.
50. van Hijfte L, Geurts M, Vallentgoed WR, *et al*. Alternative normalization and analysis pipeline to address systematic bias in NanoString GeoMx Digital Spatial Profiling data. *iScience* 2023; **26:** 105760.
51. Bolstad BM, Irizarry RA, Åstrand M, *et al*. A comparison of normalization methods for high density oligonucleotide array data based on variance and bias. *Bioinformatics* 2003; **19:** 185–193.
52. Smyth GK. Linear models and empirical Bayes methods for assessing differential expression in microarray experiments. *Stat Appl Genet Mol Biol* 2004; **3:** 3.
53. Smyth GK, Michaud J, Scott HS. Use of within-array replicate spots for assessing differential expression in microarray experiments. *Bioinformatics* 2005; **21:** 2067–2075.
54. Barbie DA, Tamayo P, Boehm JS, *et al*. Systematic RNA interference reveals that oncogenic *KRAS*-driven cancers require TBK1. *Nature* 2009; **462:** 108–112.
55. Shannon P, Markiel A, Ozier O, *et al*. Cytoscape: a software environment for integrated models of biomolecular interaction networks. *Genome Res* 2003; **13:** 2498–2504.
56. Heer J, Card SK, Landay JA. Prefuse: a toolkit for interactive information visualization. In Proceedings of the SIGCHI Conference on Human Factors in Computing Systems *(*CHI'05*)*. Association for Computing Machinery: New York, NY, 2005; 421–430.
57. Utriainen M, Morris JH. *clusterMaker2*: a major update to *clusterMaker*, a multi-algorithm clustering app for Cytoscape. *BMC Bioinformatics* 2023; **24:** 134.

References 50–57 are cited only in the supplementary material.

SUPPLEMENTARY MATERIAL ONLINE

Supplementary materials and methods

Figure S1. GeoMx sample slide preparation

Figure S2. Sample re-grouping

Figure S3. UMAP plots according to the patient and medication status

Figure S4. Tissue staining of ANO7 and immune cells

Figure S5. Network analysis

Figure S6. *ANO7* expression in TCGA PRAD bulk RNA-seq per sample group

Figure S7. Immune cell analysis

Figure S8. Signal-to-noise ratio and data distribution (referred to in Supplementary materials and methods)

Table S1. Clinical information of the patients (referred to in Supplementary materials and methods)

Table S2. Differentially expressed genes per group

Table S3. Gene-set enrichment analysis

Table S4. Differentially expressed genes per individual patient in low inflammation regions

Table S5. Correlation coefficients calculated in pos-norm samples for DEGs upregulated in pos-norm per patient

Table S6. ClueGO network analysis

Table S7. *ANO7* correlation signatures in TCGA PRAD per Gleason score group

Table S8. Pathway enrichment analysis for TCGA PRAD *ANO7* correlation signatures per sample group

Table S9. Cell type gene markers used in ssGSEA (referred to in Supplementary materials and methods)